OCEANOGRAPHY

Glacial carbon cycle changes by Southern Ocean processes with sedimentary amplification

Hidetaka Kobayashi[1]*, Akira Oka[1], Akitomo Yamamoto[2], Ayako Abe-Ouchi[1]

Recent paleo reconstructions suggest that increased carbon storage in the Southern Ocean during glacial periods contributed to low glacial atmospheric carbon dioxide concentration (pCO$_2$). However, quantifying its contribution in three-dimensional ocean general circulation models (OGCMs) has proven challenging. Here, we show that OGCM simulation with sedimentary process considering enhanced Southern Ocean salinity stratification and iron fertilization from glaciogenic dust during glacial periods improves model-data agreement of glacial deep water with isotopically light carbon, low oxygen, and old radiocarbon ages. The glacial simulation shows a 77-ppm reduction of atmospheric pCO$_2$, which closely matches the paleo record. The Southern Ocean salinity stratification and the iron fertilization from glaciogenic dust amplified the carbonate sedimentary feedback, which caused most of the increased carbon storage in the deep ocean and played an important role in pCO$_2$ reduction. The model-data agreement of Southern Ocean properties is crucial for simulating glacial changes in the ocean carbon cycle.

INTRODUCTION

Atmospheric carbon dioxide concentration (pCO$_2$) during the Last Glacial Maximum (LGM) was lower by about 90 parts per million (ppm) than during the late Holocene (1). Although the accumulation of more carbon in the ocean during glacial periods is recognized as a major factor (2), the detailed mechanism behind the atmospheric pCO$_2$ change is not fully understood. Paleo reconstructions indicate that physical and biogeochemical changes in the Southern Ocean are essential for ocean carbon uptake during glacial periods (3, 4). It is also suggested that saline and cold (temperatures near freezing) bottom water occupies the Southern Ocean during LGM (5). Furthermore, radiocarbon ages in the glacial deep South Atlantic are shown to be by more than 1000 ^{14}C years older than the late Holocene (6). Although there are uncertainties in reconstructing high deep-sea salinity (7, 8) and radiocarbon ages (6), these studies imply a stronger salinity stratification and a more isolated deep ocean in the glacial Southern Ocean than in the late Holocene.

Previous modeling studies have attempted to explain the glacial-interglacial changes in atmospheric pCO$_2$, but the quantitative contributions of individual processes are controversial. Several studies with Earth System Models of Intermediate Complexity (EMICs) have successfully explained the glacial changes in atmospheric pCO$_2$, such as the CLIMBER-2 model (9–11), which includes a two-dimensional ocean model, and the Bern3D model (12), which includes a three-dimensional ocean model. However, evaluations of the reproducibility of glacial changes in physical and biogeochemical oceanic processes are insufficient. Their discussion is limited to model-data comparisons of global average or vertical one-dimensional biogeochemical properties (9–11), and the results highly depend on how the ocean processes are parameterized and represented. On the other hand, more complex three-dimensional ocean general circulation models (OGCMs) generally have difficulty reproducing all the amplitude of the changes in atmospheric pCO$_2$ by imposing well-known forcing of ocean temperature, salinity, ocean circulation, sea ice, iron fertilization, and inorganic carbonate chemistry during glacial periods (13–17). One reason for this is the insufficient model-data agreement of the Southern Ocean

during glacial periods (18). Model-data agreement of the glacial high deep-sea salinity in the Southern Ocean is relatively low in most OGCMs (19). It may be related to the unrealistic representation of shelf processes, such as open-ocean deep convection around Antarctica, due to the limited spatial resolution of global ocean modeling (20).

On the basis of the literature, we previously demonstrated that model-data agreement of the glacial carbon cycle could improve by considering the contributions of enhanced Southern Ocean salinity stratification with carbonate compensation (18) and iron fertilization from glaciogenic dust (21). These contributions have not been adequately considered in previous OGCM studies. However, the relative importance of these processes is not fully understood, and we did not include comprehensive comparisons with available paleo data in our previous studies. Previous OGCM studies assessed model-data comparisons of three-dimensional carbon isotopes (22–26). Some of these studies have evaluated the impact of different processes on atmospheric pCO$_2$ and/or oceanic carbon reservoirs. However, most of these studies focused primarily on the impact of differences in the Atlantic meridional overturning circulation (AMOC) on carbon isotopes and did not simultaneously assess the processes described above (i.e., the enhanced Southern Ocean salinity stratification, carbonate compensation, and iron fertilization from glaciogenic dust).

Here, we used a three-dimensional OGCM with ocean sedimentary process to perform glacial carbon cycle simulations, considering both enhanced Southern Ocean salinity stratification (18) and iron fertilization from glaciogenic dust (21). We report comprehensive comparisons with available paleo data about the ocean biogeochemical properties (dissolved oxygen, δ^{13}C, and radiocarbon ages). We assessed each process's contribution to the model-data agreement of glacial water masses and changes in atmospheric pCO$_2$ by performing sensitivity simulations focusing on the stratified Southern Ocean and glaciogenic dust. The model used, the spin-up process, the experimental design, and the processes considered regarding carbonate compensation are described in Materials and Methods.

RESULTS

LGM water mass distribution

We first conducted control simulations under the conditions of pre-industrial (PI) and LGM, named PI_ctl and LGM_ctl, respectively

[1]Atmosphere and Ocean Research Institute, The University of Tokyo, Kashiwa, Japan. [2]Japan Agency for Marine-Earth Science and Technology, Yokohama, Japan.
*Corresponding author. Email: hidekoba@aori.u-tokyo.ac.jp

(see Materials and Methods and table S1). Note that LGM_ctl is a standard LGM simulation and includes processes usually considered to be glacial conditions (e.g., temperature, salinity, circulation, and non-glaciogenic dust deposition). In addition, PI_ctl and LGM_ctl are the same as those reported in the authors' previous study (18). We then conducted additional simulations to evaluate both the individual impacts of enhanced Southern Ocean salinity stratification (LGM_strat), iron fertilization from glaciogenic dust (LGM_glac), and their combined impact (LGM_so). We also performed the simulations considering carbonate compensation on the ocean carbon cycle (LGM_all), in which the ocean-sediment model (18) was explicitly coupled to the OGCM (see Materials and Methods). On the basis of the simulation results, Fig. 1 summarizes the contributions of the additional processes (i.e., the stratified Southern Ocean, glaciogenic dust, and carbonate sedimentary processes) to global changes in atmospheric pCO$_2$ and ocean biogeochemical properties (dissolved oxygen, δ^{13}C, and radiocarbon ages), as well as their changes in the control simulation (LGM_ctl).

As for glacial changes in dissolved oxygen, the LGM_ctl simulation qualitatively reproduced the glacial changes such as oxygen decline in most of the ocean below 1000 m (circles in Fig. 2, A and B). However, these changes were underestimated relative to quantitative reconstruction (triangles in Fig. 2, A and B), especially in the Southern Ocean; the globally averaged dissolved oxygen below 1000 m decreased from PI_ctl by 22.4 mmol m^{-3}, while the corresponding average of six proxy records is 67.8 mmol m^{-3} (LGM control in Fig. 1B; table S2). On the other hand, the LGM_all simulation showed more than 100 mmol m^{-3} oxygen decline in the Southern Ocean and better agreement with the paleo reconstructions (Fig. 2, C and D). The globally averaged dissolved oxygen below 1000 m decreased from PI_ctl by 77.5 mmol m^{-3} (total changes in Fig. 1B; table S2), and the root mean square error (RMSE) of the glacial change with the data decreased to 33.7 mmol m^{-3} from 51.3 mmol m^{-3} in LGM_ctl (table S5). More than half of this global oxygen reduction came from the stratified Southern Ocean (stratified SO in Fig. 1B). Especially in the deep South Atlantic (Fig. 2C), the simulated deoxygenation was substantially larger than in the previous study, which included only the effects of glaciogenic dust (21). Although this is still smaller than the estimated change of 175 mmol m^{-3} (27), the foraminifera species used in this reconstruction have not been fully validated, and some studies suggest that the deoxygenation may be overestimated (28). Therefore, we believe that the oxygen changes were well simulated in the LGM_all simulation and came mainly from the Southern Ocean salinity stratification.

For the glacial changes in δ^{13}C, the LGM_all simulation reproduced the large decline of δ^{13}C in the deep ocean, especially in the South Atlantic (Fig. 3C). Previous model-data comparisons of carbon isotopes have shown that a shallower and weaker flow of North Atlantic Deep Water (NADW) than that in the preindustrial is necessary to simulate their pattern in LGM (22–24). Our results support this idea but suggest that this was not sufficient in LGM_ctl (Fig. 3A and fig. S6). The enhanced Southern Ocean salinity stratification was essential for reproducing low δ^{13}C in the South Atlantic. This view is consistent with a previous study showing that reduced ventilation in the deep Southern Ocean improved model-data agreement of δ^{13}C (23). The globally averaged glacial change of δ^{13}C was −0.56‰, which is sufficiently low compared to the −0.19‰ of LGM_ctl but is almost the upper limit of the reported estimate of −0.34 ± 0.19‰ (29) (total changes in Fig. 1C; table S3). Half of this change is estimated

to have come from the contribution of enhanced salinity stratification (Stratified SO in Fig. 1C). The efficient biological pump, due to iron fertilization from glaciogenic dust, also somewhat contributed to lowering δ^{13}C (13% of the total change; glaciogenic dust in Fig. 1C). The large decline in δ^{13}C compared to the paleo data in the deep Pacific contributed to the slight overestimation of global changes (Fig. 3D). In the LGM_all simulation, the correlation with the global reconstructions was 0.79 and RMSE was 0.32‰ (table S4), which are comparable with previous studies of 0.79 and 0.33‰ (24) and 0.80 and 0.36‰ (26). These modeling studies, including our LGM_all simulation, suggest a weaker LGM NADW (22–24). In contrast, a data assimilation study suggests a more vigorous LGM AMOC (25). A recent study points out that geometry is more important than strength in terms of consistency with δ^{13}C data (26). Although our results support the shallower and weaker LGM NADW for explaining the distribution of δ^{13}C, further analysis in combination with ocean tracers such as ^{231}Pa/^{230}Th and ϵ_{Nd} is expected to lead to a more detailed understanding of LGM AMOC. Without salinity stratification in the Southern Ocean, some studies successfully reproduce δ^{13}C during LGM (24, 30). These OGCM studies suggest that weaker NADW and enhanced export production due to iron fertilization are responsible for lower δ^{13}C in the glacial Atlantic Ocean. The contribution of a particular process to the model-data agreement may depend on the model used.

For the glacial changes in Δ^{14}C, the LGM_all simulation reproduced the very old radiocarbon ages in the deep North Atlantic (Fig. 4C), which appears to be partly due to the weakening of NADW. The old deep water was also simulated in the Southern Ocean around Antarctica and was consistent with paleo data (Fig. 4, C and D). More than 40% of the global change in radiocarbon ages came from the enhanced Southern Ocean salinity stratification (Stratified SO in Fig. 1D). We found that the radioactive decay of ^{14}C in ocean sediments and its leak into the bottom ocean, which are usually neglected, contributed somewhat to older radiocarbon ages in the glacial ocean (nearly 80 ^{14}C years; sedimentary processes in Fig. 1D). However, this sedimentary response may be overestimated, as discussed later. As a result, the global average of radiocarbon ages increased by 667 ^{14}C years (total changes in Fig. 1D; table S3) when taking these factors into account, close to the paleo ^{14}C data of 689 ± 53 ^{14}C years (6). We also note the differences between radiocarbon and ideal ages. The increased disequilibrium during the air-sea gas exchange enlarges radiocarbon ages during glacial periods, but this process does not affect ideal ages (31). The glacial increase in globally averaged surface radiocarbon age in the upper 100 m was 394 ^{14}C years (463 ^{14}C years in PI_ctl and 857 ^{14}C years in LGM_all), which also contributed to older radiocarbon ages in the deep glacial ocean. Some studies have shown that the disequilibrium CO$_2$ change is an important process for explaining the global change of radiocarbon ages during LGM (30, 32). In contrast, the contribution of disequilibrium CO$_2$ alone in this study was small compared to the estimated global change. Although the estimation of radiocarbon ages contains high uncertainty [about 620 ^{14}C years; (6)], the global change in LGM_all is one of the most consistent with paleo data among the previously reported OGCM studies. In LGM_all, RMSE decreased to 592 ^{14}C years from 612 ^{14}C years in LGM_ctl (table S4). A previous OGCM study reported a global change of 635 ^{14}C years and RMSE of about 710 ^{14}C years under shallower and weaker glacial NADW conditions (24); the present results are consistent with that study under the realistic model settings. In addition to shallower and weaker glacial
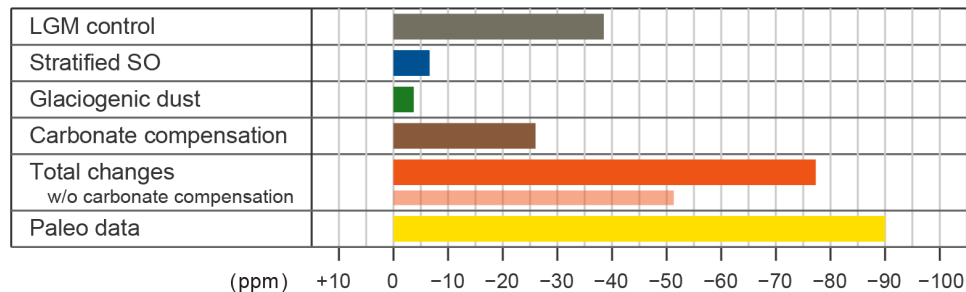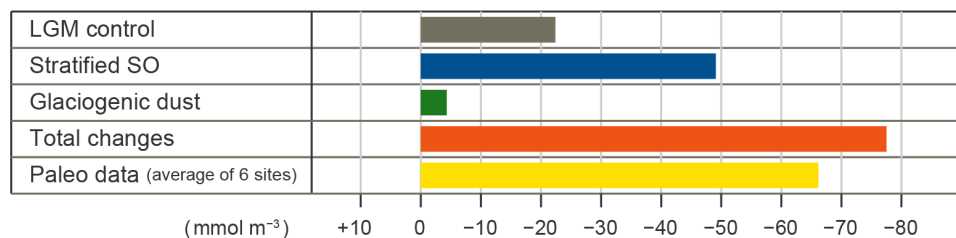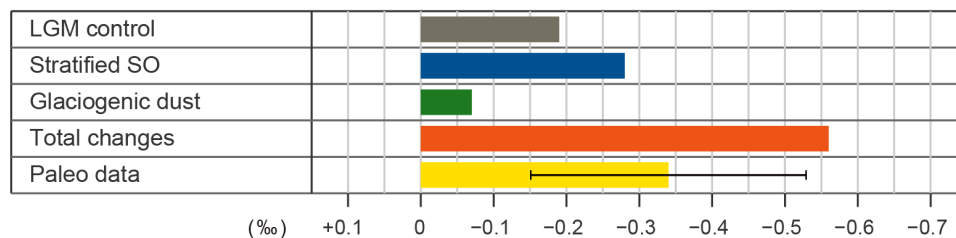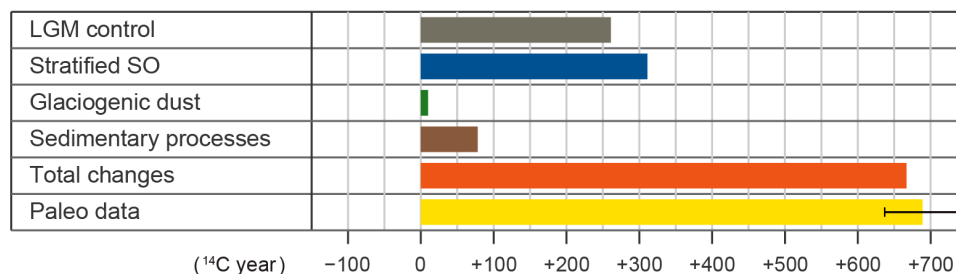
Fig. 1. Processes contributing to glacial changes in atmospheric pCO_2 and ocean properties. The contribution of individual processes to the global change in (**A**) atmospheric pCO_2 (ppm), (**B**) dissolved oxygen below 1000 m (mmol m^{-3}), (**C**) δ^{13}C (‰), and (**D**) radiocarbon ages (^{14}C year) from the preindustrial control simulation (PI_ctl) to the LGM_all simulation, which includes all the processes considered in this study under the LGM climate ("Total changes"; orange), is shown with global paleo records (yellow) of dissolved oxygen (table S6), δ^{13}C (29), and radiocarbon ages (6). The impact of a particular process (i.e., enhanced salinity stratification in the Southern Ocean, iron fertilization from glaciogenic dust, and carbonate sedimentary process) is evaluated by the difference between the LGM_so simulation and the simulation without (or with) the process. "Stratified SO" shows the contribution of enhanced salinity stratification in the Southern Ocean (SO) and is the difference between LGM_glac and LGM_so (blue). "Glaciogenic dust" shows the contribution of iron fertilization from glaciogenic dust and is the difference between LGM_strat and LGM_so (green). "Carbonate compensation (sedimentary process)" shows the contribution of carbonate sedimentary processes and is the difference between LGM_all and LGM_so (brown). "LGM control" is the change from PI_ctl to LGM_ctl (gray). Simulation results are summarized in tables S2 and S3.

NADW, as shown in previous studies (23, 24), we demonstrated that the strongly stratified Southern Ocean with sedimentary amplification is essential to explaining the glacial changes in radiocarbon ages.

Glacial changes in atmospheric pCO_2

Here, we show the changes in atmospheric pCO_2 and discuss the processes that contributed to them. As reported in our previous study (31), the changes in atmospheric pCO_2 between LGM_ctl and PI_ctl
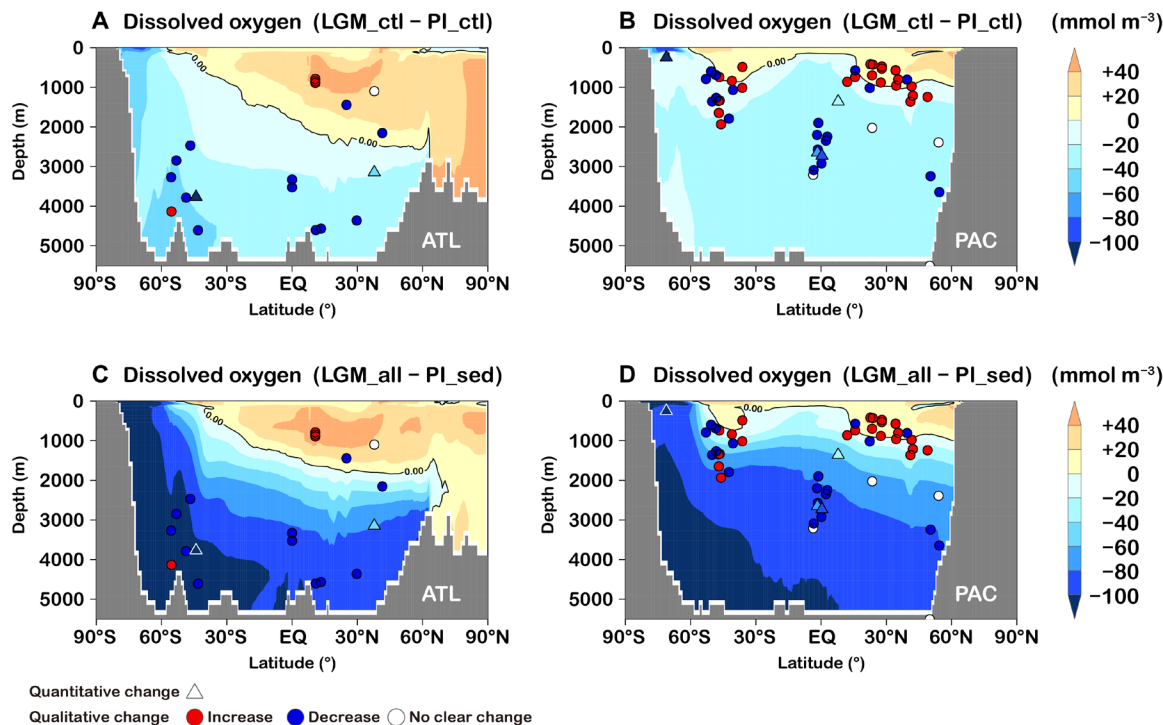
Fig. 2. Glacial changes in dissolved oxygen. Model-data comparisons of zonal mean changes in dissolved oxygen (mmol m^{-3}) from PI_ctl to LGM_ctl in the (**A**) Atlantic and (**B**) Pacific. The quantitative (triangles) and qualitative (circles) changes for dissolved oxygen estimated from paleo records are shown in table S6. (**C** and **D**) Same as (A) and (B) except for changes from PI_sed to LGM_all.
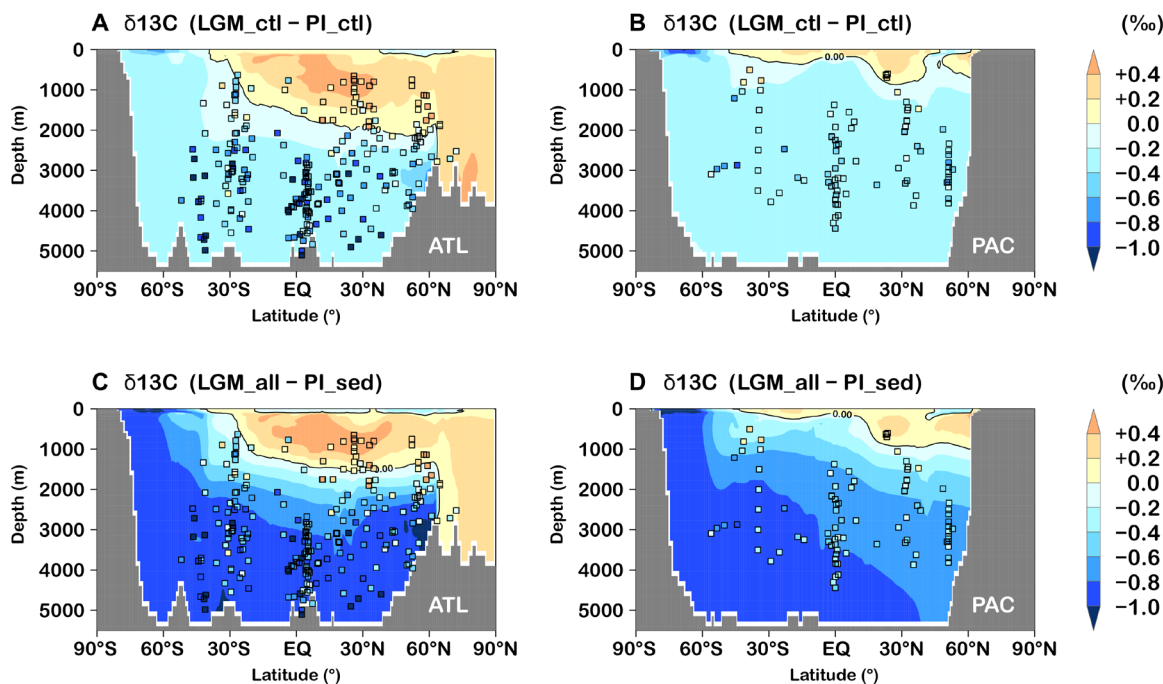
Fig. 3. Glacial changes in δ^{13}C. Model-data comparisons of zonal mean changes in δ^{13}C (‰) from PI_ctl to LGM_ctl in the (**A**) Atlantic and (**B**) Pacific with paleo records (squares) (*29*). (**C** and **D**) Same as (A) and (B) except for changes from PI_sed to LGM_all.
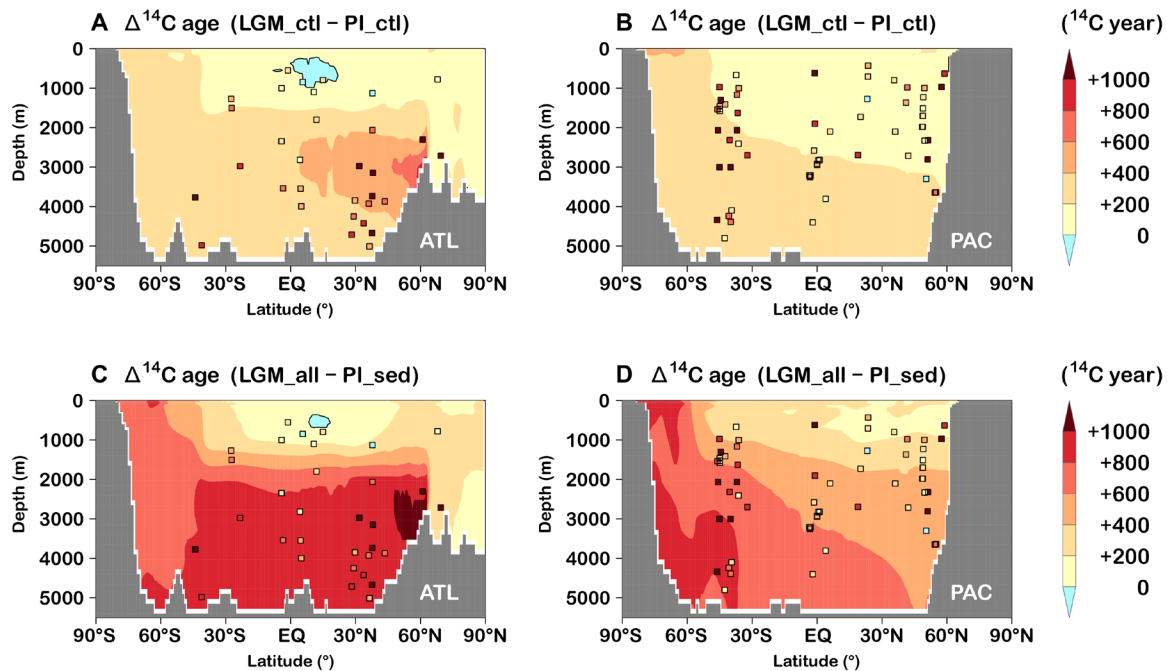
Fig. 4. Glacial changes in radiocarbon ages. Model-data comparisons of zonal mean changes in radiocarbon ages (^{14}C year) from PI_ctl to LGM_ctl in the (**A**) Atlantic and (**B**) Pacific with paleo records (squares) (6). (**C** and **D**) Same as (A) and (B) except for changes from PI_sed to LGM_all.

(−38.5 ppm; table S2) were caused by various processes: e.g., the increase in CO_2 solubility due to surface cooling, the increase in the vertical gradient of dissolved inorganic carbon (DIC) and alkalinity due to shallower and weaker NADW, and changes in biological pumps. Note that we included changes in non-glaciogenic dust deposition between LGM and late Holocene in LGM_ctl, which were among one of the most important processes causing glacial changes in biological pumps. For details about the difference between LGM_ctl and PI_ctl, please refer to our previous paper (31). In this study, we focus mainly on the LGM_all simulation. We evaluated how the additional processes (i.e., the stratified Southern Ocean, glaciogenic dust, and carbonate compensation) contributed to the glacial pCO_2 reduction.

When considering both the stratified Southern Ocean and iron fertilization from glaciogenic dust, the simulated glacial change in atmospheric pCO_2 was 51.3 ppm (total changes without carbonate compensation; pale orange bar in Fig. 1A). This response was larger than that in the LGM_ctl simulation by 12.8 ppm (LGM control in Fig. 1A). The contribution of the enhanced Southern Ocean salinity stratification was 6.6 ppm (Stratified SO in Fig. 1A) and that of the iron fertilization from glaciogenic dust was 3.7 ppm (glaciogenic dust in Fig. 1A). As for the salinity stratification, because of the Southern Ocean changes and the associated weakening of the NADW (fig. S6), the vertical gradient of nutrients and DIC became stronger; nutrients and DIC in the upper overturning cell in the Atlantic decreased, and those in the lower overturning cell increased. However, this redistribution of DIC was partially offset by decreased export production due to reduced nutrient supply (table S2 and fig. S7). As a result, the change in atmospheric pCO_2 by introducing the salinity stratification became moderate. As for the iron fertilization from glaciogenic dust, this process reduced iron limitation and increased export production in the sub-Antarctic region, consistent with the qualitative

changes estimated from proxies (fig. S7), which reduced atmospheric pCO_2. These processes contributed to the increased respired carbon in the Southern Ocean as inferred from oxygen and $\delta^{13}C$ described in the previous section.

When we considered the sedimentation process, the carbonate compensation further enhanced the glacial reduction of atmospheric pCO_2 (because this process takes a long time to reach a steady state, we performed several spin-up simulations to obtain the final steady state; see the time series of our spin-up simulations in fig. S13). With the stratified Southern Ocean and iron fertilization from glaciogenic dust, our results demonstrated that the carbonate compensation controlled the total inventory of ocean alkalinity in response to the redistribution of DIC and alkalinity in the ocean interior, further reducing atmospheric pCO_2. Consequently, the glacial reduction of atmospheric pCO_2 in LGM_all reached 77.3 ppm (total changes in Fig. 1A) and was close to the observed 90 ppm. This final response is one of the largest responses among the previously reported GCM studies (13–18, 21) and is comparable to a recently reported 67 to 87 ppm (30).

When we included the carbonate sedimentary process ("Open System" in fig. S13), there was a net increase in ocean carbon and alkalinity in all the LGM simulations (fig. S13, C and D), as the carbonate compensation relaxed the imbalance between the carbonate inflow from rivers and the carbonate removal by sediment burial (fig. S13B). This adjustment facilitated CO_2 uptake at the surface ocean and further reduced atmospheric pCO_2 (fig. S13A). The total impact of carbonate compensation on atmospheric pCO_2 was approximately 26.0 ppm (carbonate compensation in Fig. 1A). Note that this response (i.e., the difference between LGM_so and LGM_all; brown bar in Fig. 1A) was larger than the difference between LGM_ctl and LGM_sed (11.5 ppm in table S2; brown bar in fig. S15A). This means that the effect of carbonate compensation became amplified

when we considered the stratified Southern Ocean and iron fertilization from glaciogenic dust. This amplification is explained below.

The carbonate compensation affected atmospheric $p\mathrm{CO_2}$ by controlling the total inventory of alkalinity in the ocean (i.e., higher alkalinity led to lower atmospheric $p\mathrm{CO_2}$). The inventory of alkalinity was determined under the balance between carbonate river inflow and carbonate burial flux. The former was assumed to be constant in our simulations; therefore, the latter was a key variable. The carbonate burial flux was mainly controlled by the carbonate flux reaching the seafloor and the degree of bottom-water carbonate saturation. Because the carbonate saturation became lower for older water masses, the stratified Southern Ocean tended to reduce the carbonate burial flux. The carbonate saturation was also affected by the dissolution of the organic matter in the sea bottom; larger dissolution of the organic matter led to lower carbonate saturation. Therefore, iron fertilization reduced carbonate burial flux by transporting respired carbon to the deep ocean, although this was partially counteracted by increased carbonate export flux. The decreased carbonate burial flux increased alkalinity in the ocean under a constant river inflow. The increased alkalinity, in turn, tended to restore the reduced carbonate burial flux, and alkalinity continued increasing until the riverine flux and carbonate burial flux were balanced again (therefore, this process is referred to as carbonate "compensation"). In summary, considering the carbonate sedimentary process enabled us to evaluate how much the total inventory of alkalinity has changed. This study clarified that the combination of the stratified Southern Ocean and iron fertilization led to a large decline in atmospheric $p\mathrm{CO_2}$ as a result of carbonate compensation. The increase of the globally averaged alkalinity in LGM_all, which considered these two processes, from PI_sed was 76.7 mmol m^{-3}, which was larger than the increase of 30.6 mmol m^{-3} in LGM_sed (fig. S13). The detailed analysis of the sedimentary processes (e.g., budget analysis of carbonate inflow and outflow in sediment layers) can be reviewed in our previous study (18).

In response to changes in $p\mathrm{CO_2}$, carbon sequestration in the ocean also increased. The increase in ocean carbon storage from the PI_ctl simulation was 732 PgC (total changes in fig. S14; table S2). This is also comparable to estimates from paleo proxy: about 850 PgC estimated from changes in oxygen (28, 33) or $\Delta^{14}\mathrm{C}$ (34) and 540 to 1040 PgC estimated from changes in $\delta^{13}\mathrm{C}$ (29, 35), while this became only 110 PgC without carbonate compensation (fig. S14; LGM_so in table S2). This is because, in the closed-system response where the sediment model was not coupled with the ocean model, the redistribution of DIC caused by changes in $\mathrm{CO_2}$ solubility, ocean circulation, biological pumps, and air-sea gas exchange increased the carbon storage in the deep ocean, but most of this increase was compensated by a decrease in carbon storage in the upper ocean. Therefore, carbonate compensation was necessary to bring about carbon sequestration in the ocean, consistent with proxies.

In summary, we found that carbonate compensation was responsible for the large glacial decrease in atmospheric $p\mathrm{CO_2}$ as a result of amplified sedimentary response due to the enhanced Southern Ocean salinity stratification and iron fertilization from glaciogenic dust. Changes in ocean carbon sequestration were also consistent with reconstructions from several proxies, supporting the validity of the simulated carbon cycle field.

DISCUSSION
Our best LGM simulation (LGM_all) showed an ~80-ppm glacial change in atmospheric $p\mathrm{CO_2}$ under multiple paleo data constraints.

Although previous modeling studies have reported that large changes in atmospheric $p\mathrm{CO_2}$ can be successfully simulated using EMIC (9–12), idealized OGCM (36), and OGCM (30), we emphasize that our LGM OGCM simulation is capable of reproducing not only large changes in atmospheric $p\mathrm{CO_2}$ but also the three-dimensional distribution of multiple paleo records (dissolved oxygen, $\delta^{13}\mathrm{C}$, and radiocarbon ages) under realistic model settings.

We have demonstrated that the model-data agreement of ocean properties in the Southern Ocean is key for properly simulating glacial changes in the ocean carbon cycle. This study applied salinity restoring and small vertical diffusivity in the Southern Ocean to reproduce the enhanced salinity stratification. This treatment is useful for more realistic LGM simulation but needs improvement so that the model can explicitly predict smaller vertical diffusivity and more saline deep water during LGM relative to the present. For example, during LGM, more appropriate treatment regarding active sea ice production and the associated brine rejection might be required for reproducing the enhanced salinity stratification. The vertical diffusivity also needs to be diagnosed in the model rather than prescribed. Some EMIC studies introduced a brine parameterization and a stratification-dependent vertical diffusion coefficient (9, 37). Applying such parameterizations to our OGCM is desirable, and we plan to explore this in future work. This would lead to a better understanding of the processes that strengthened salinity stratification and evaluated the influence of changes in thermal stratification on vertical diffusivity. Several studies have pointed out the importance of tidal mixing on the glacial AMOC (38, 39), and it might be interesting to investigate its role in the ocean carbon cycle.

This study assumed that LGM was in a steady state as in previous GCM studies; however, the validity of this steady-state assumption needs to be discussed in future studies. Because the time scale of carbonate compensation is very long, the steady-state assumption tends to overestimate its actual response. Furthermore, the response of terrestrial carbon reservoirs is also partially responsible for transient changes in the glacial-interglacial carbon cycle. Recently, transient changes in the ocean carbon cycle during the last deglaciation began to be evaluated with EMICs (10–12, 37, 40, 41). Our MIROC coupled model was reportedly able to reproduce the changes in AMOC during the last deglaciation, consistent with proxy data (42). It would be an interesting future study to perform transient deglaciation simulations of the carbon cycle using our OGCM.

MATERIALS AND METHODS
Model description
The OGCM used in this study was COCO version 4.0 (43). The horizontal resolution was about 1°, and the model had 43 layers (5 to 250 m). We took sea surface boundary conditions from the outputs of the atmosphere-ocean general circulation model MIROC 4m (44, 45). We obtained the initial condition of ocean temperature and salinity from Polar Science Center Hydrographic Climatology (46).

Ocean carbon cycle simulations were conducted by imposing the precalculated ocean physical fields using an offline ocean biogeochemical model based on a previous study including the iron cycle (16, 31, 47). The prognostic variables were phosphate, DIC, alkalinity, dissolved organic phosphate, dissolved oxygen, iron, and silicate. The uptake rate of phosphate by phytoplankton was determined by light, phosphate, and iron availability. The air-borne iron flux was assumed to be 3.5 weight % of total dust deposition (48). We took

the initial distribution of ocean biogeochemical tracers from the climatology of World Ocean Atlas 2001 (49, 50) and the Global Ocean Data Analysis Project (51). The initial iron concentration was a constant value of 0.6 nmol. The model included a well-mixed one-box atmosphere. Atmospheric pCO_2 was predicted by the gas exchange between the sea surface and the atmosphere box. Atmospheric $\delta^{13}C$ and $\Delta^{14}C$ were fixed at −6.5 and 0‰, respectively.

The ocean-sediment model used in this study is the same one used in our previous study (18), which was created on the basis of previous studies (52–54). The sediment layer was 10 cm and was divided into 10 layers. The prognostic variables were clay, particulate organic carbon, calcium carbonate, and biogenic silica in solids, and phosphate, DIC, alkalinity, dissolved oxygen, and silicate in solutes. The boundary condition was particle flux reaching the seabed and bottom-water concentrations of solutes. The model parameters were referenced from previous studies except that the dissolution constant of calcium carbonate was set to 7.5×10^{-6} day^{-1} which was chosen for realistically simulating the total burial rate of carbonate in our model.

Carbonate sedimentary processes

When the sediment model was coupled with the ocean model, calcium carbonates that settled down the water column and reached the seabed flowed into the sedimentary layer. In upper sediments, carbonates dissolved when unsaturated, depending on the conditions of pore water. The remaining undissolved carbonates were treated as being buried for a long time and were removed from the ocean-sediment system. Because carbonates were removed from the bottom of the sedimentary layer, the river inflow of carbonates was needed. Carbonate compensation was the feedback that worked to balance the river inflow and the burial removal of carbonates. Under glacial conditions, carbon accumulation caused deep water to become acidic and promoted the dissolution of carbonates. Because of the imbalance between the river inflow and burial removal (i.e., the river inflow was larger than the burial removal of carbonates), DIC and alkalinity in the entire ocean increased at a ratio of 1:2. This inventory change made carbonates less soluble, and the imbalance was relaxed after a 10,000-year scale adjustment. We also calculated ^{13}C and ^{14}C contained in carbonate sediments. Radioactive decay of ^{14}C in the sediments decreased ^{14}C in pore water by the dissolution of carbonates. Thus, the exchange of properties at the sediment-water interface decreased ^{14}C in the water column. On the other hand, there was no fractionation of ^{13}C by the formation and dissolution of carbonates. Because this study only focused on the sedimentary process of calcium carbonate, the distribution of nutrients, silicates, and oxygen did not change with or without the coupling of the sediment model. Accordingly, global export of organic matter, calcium carbonate, and biogenic silica also did not change because they depend on the surface ocean's availability.

Spin-up

We performed three spin-up steps in this study to evaluate the steady-state response of the ocean carbon cycle including ocean sediments. First, we conducted steady-state simulations for ocean biogeochemical tracers using the offline ocean biogeochemical model for 20,000 years (Closed System in fig. S13). During this Closed-System spin-up, the inventory of ocean tracers did not change. Biogenic particles arriving at the sediment-water interface dissolved immediately. Next, we conducted steady-state simulations for ocean-sediment tracers using

the ocean-sediment model for 150,000 years under the boundary conditions at the sediment-water interface taken from the above-obtained ocean biogeochemical fields. The sediment model run aimed to create an initial sedimentary field for coupling spin-up using the OGCM with the sediment model. Different sediment compositions were obtained in each simulation, depending on particle fluxes and bottom-water properties at the sediment-water interface. Third, we conducted a spin-up using both the offline ocean biogeochemical model and the ocean-sediment model initialized from the above-obtained ocean and sediment biogeochemical fields (Open System in fig. S13). This Open-System spin-up was further divided into two steps. We first calculated only the change in ocean average tracer concentration due to the imbalance of riverine input and burial of calcium carbonate. This spin-up was conducted to reduce the computational cost required for long-term steady-state integration. After that, a spin-up of the fully coupled ocean and sediment models was conducted for 40,000 years. In the Open-System spin-up, the total inventory and spatial distribution of DIC and alkalinity changed at a ratio of 1:2, as carbonates flowed into and out of the ocean. The riverine flux of calcium carbonate was the same as the burial of calcium carbonate obtained in the sediment-only spin-up of preindustrial control simulations. The details of the spin-up, including the sediment model, were the same as in our previous study (18), except for the integration time.

Experimental design

We first conducted control simulations under the conditions of preindustrial and LGM climates, named PI_ctl and LGM_ctl, respectively. The ocean physical boundary conditions of PI_ctl and LGM_ctl were obtained from OGCM simulations under each climate. Dust deposition of PI_ctl and LGM_ctl was taken from the results of preindustrial and LGM simulation using the atmospheric aerosol transport model of SPRINTARS (55), respectively. The iron solubility in the desert dust was assumed to be 1%. We then conducted additional simulations to evaluate the impacts of the enhanced Southern Ocean salinity stratification (LGM_strat), the iron fertilization from glaciogenic dust (LGM_glac), and their combination (LGM_so). We also performed simulations that considered the sedimentary response of carbonates on the ocean carbon cycle to LGM_ctl (LGM_sed) and LGM_so (LGM_all). In these simulations, the ocean-sediment model (18) was explicitly coupled to the OGCM. In LGM_strat, we applied salinity restoring toward high salinity in the bottom layer around Antarctica to mimic deep-water formation and improved the model-data agreement of the high deep-sea salinity reported from paleo data (5, 56). The restoring was carried out assuming a deep-water formation area, approaching 37 PSU (practical salinity unit) in the Weddell Sea and the Ross Sea and 38 PSU in the East Antarctic Ocean. Furthermore, to consider weaker vertical mixing resulting from stronger salinity stratification, we set a small vertical diffusivity (0.1 cm^2 s^{-1}) in the Southern Ocean south of 30ºS (31). In LGM_glac, in addition to the original dust input in LGM_ctl, the air-borne iron flux from glaciogenic dust was applied (57), where the iron solubility from glaciogenic dust was assumed to be 3% (21). In LGM_so, both additional processes in LGM_strat and LGM_glac were considered. In LGM_sed and LGM_all, we evaluated the sedimentary response by coupling a sediment model to the ocean biogeochemical model. LGM_all (LGM_sed) was a simulation with the same settings as LGM_so (LGM_ctl), except that the carbonate sedimentary process was included. That is, LGM_all considered the carbonate sedimentary

process under the glacial ocean conditions with the enhanced Southern Ocean salinity stratification and the iron fertilization from glaciogenic dust. We also ran the PI_sed simulation, a reference simulation for the preindustrial in the cases coupled with a sediment model. Note that changes in terrestrial carbon reservoirs were not explicitly simulated in any of our simulations. Specifically, no change in the terrestrial carbon reservoir was assumed in our Closed System simulation, whereas changes in the terrestrial carbon reservoir became equivalent to changes in ocean (plus atmosphere) carbon inventory in our Open System simulation. Table S1 summarizes the experimental design.

SUPPLEMENTARY MATERIALS

Supplementary material for this article is available at http://advances.sciencemag.org/cgi/content/full/7/35/eabg7723/DC1

REFERENCES AND NOTES

1. D. Lüthi, M. Le Floch, B. Bereiter, T. Blunier, J.-M. Barnola, U. Siegenthaler, D. Raynaud, J. Jouzel, H. Fischer, K. Kawamura, T. F. Stocker, High-resolution carbon dioxide concentration record 650,000–800,000 years before present. *Nature* **453**, 379–382 (2008).
2. W. S. Broecker, Glacial to interglacial changes in ocean chemistry. *Prog. Oceanogr.* **11**, 151–197 (1982).
3. D. M. Sigman, M. P. Hain, G. H. Haug, The polar ocean and glacial cycles in atmospheric CO_2 concentration. *Nature* **466**, 47–55 (2010).
4. J. W. B. Rae, A. Burke, L. F. Robinson, J. F. Adkins, T. Chen, C. Cole, R. Greenop, T. Li, E. F. M. Littley, D. C. Nita, J. A. Stewart, B. J. Taylor, CO_2 storage and release in the deep Southern Ocean on millennial to centennial timescales. *Nature* **562**, 569–573 (2018).
5. J. F. Adkins, K. McIntyre, D. P. Schrag, The salinity, temperature, and $\delta^{18}O$ of the glacial deep ocean. *Science* **298**, 1769–1773 (2002).
6. L. C. Skinner, F. Primeau, E. Freeman, M. de la Fuente, P. A. Goodwin, J. Gottschalk, E. Huang, I. N. McCave, T. L. Noble, A. E. Scrivner, Radiocarbon constraints on the glacial ocean circulation and its impact on atmospheric CO_2. *Nat. Commun.* **8**, 16010 (2017).
7. M. D. Miller, M. Simons, J. F. Adkins, S. E. Minson, The information content of pore fluid $\delta^{18}O$ and [Cl⁻]. *J. Phys. Oceanogr.* **45**, 2070–2094 (2015).
8. C. Wunsch, Pore fluids and the LGM ocean salinity—Reconsidered. *Quat. Sci. Rev.* **135**, 154–170 (2016).
9. N. Bouttes, D. Paillard, D. M. Roche, V. Brovkin, L. Bopp, Last glacial maximum CO_2 and $\delta^{13}C$ successfully reconciled. *Geophys. Res. Lett.* **38**, L02705 (2011).
10. V. Brovkin, A. Ganopolski, D. Archer, G. Munhoven, Glacial CO_2 cycle as a succession of key physical and biogeochemical processes. *Clim. Past* **8**, 251–264 (2012).
11. A. Ganopolski, V. Brovkin, Simulation of climate, ice sheets and CO_2 evolution during the last four glacial cycles with an Earth system model of intermediate complexity. *Clim. Past* **13**, 1695–1716 (2017).
12. L. Menviel, F. Joos, S. P. Ritz, Simulating atmospheric CO_2, ^{13}C and the marine carbon cycle during the last glacial-interglacial cycle: Possible role for a deepening of the mean remineralization depth and an increase in the oceanic nutrient inventory. *Quat. Sci. Rev.* **56**, 46–68 (2012).
13. L. Bopp, K. E. Kohfeld, C. Le Quéré, O. Aumont, Dust impact on marine biota and atmospheric CO_2 during glacial periods. *Paleoceanography* **18**, 1046 (2003).
14. T. Kurahashi-Nakamura, A. Abe-Ouchi, Y. Yamanaka, K. Misumi, Compound effects of Antarctic sea ice on atmospheric pCO_2 change during glacial-interglacial cycle. *Geophys. Res. Lett.* **34**, L20708 (2007).
15. A. Tagliabue, L. Bopp, D. M. Roche, N. Bouttes, J.-C. Dutay, R. Alkama, M. Kageyama, E. Michel, D. Paillard, Quantifying the roles of ocean circulation and biogeochemistry in governing ocean carbon-13 and atmospheric carbon dioxide at the last glacial maximum. *Clim. Past* **5**, 695–706 (2009).
16. A. Oka, A. Abe-Ouchi, M. O. Chikamoto, T. Ide, Mechanisms controlling export production at the LGM: Effects of changes in oceanic physical fields and atmospheric dust deposition. *Global Biogeochem. Cycles* **25**, GB2009 (2011).
17. M. O. Chikamoto, A. Abe-Ouchi, A. Oka, R. Ohgaito, A. Timmermann, Quantifying the ocean's role in glacial CO_2 reductions. *Clim. Past* **8**, 545–563 (2012).
18. H. Kobayashi, A. Oka, Response of atmospheric pCO_2 to glacial changes in the Southern Ocean amplified by carbonate compensation. *Paleoceanography* **33**, 1206–1229 (2018).
19. B. L. Otto-Bliesner, C. D. Hewitt, T. M. Marchitto, E. Brady, A. Abe-Ouchi, M. Crucifix, S. Murakami, S. L. Weber, Last Glacial Maximum ocean thermohaline circulation: PMIP2 model intercomparisons and data constraints. *Geophys. Res. Lett.* **34**, L12706 (2007).
20. C. Heuzé, Antarctic bottom water and north atlantic deep water in CMIP6 models. *Ocean Sci.* **17**, 59–90 (2021).
21. A. Yamamoto, A. Abe-Ouchi, R. Ohgaito, A. Ito, A. Oka, Glacial CO_2 decrease and deep-water deoxygenation by iron fertilization from glaciogenic dust. *Clim. Past* **15**, 981–996 (2019).
22. T. Hesse, M. Butzin, T. Bickert, G. Lohmann, A model-data comparison of $\delta^{13}C$ in the glacial Atlantic Ocean. *Paleoceanography* **26**, PA3220 (2011).
23. L. Menviel, J. Yu, F. Joos, A. Mouchet, K. J. Meissner, M. H. England, Poorly ventilated deep ocean at the Last Glacial Maximum inferred from carbon isotopes: A data-model comparison study. *Paleoceanography* **32**, 2–17 (2017).
24. J. Muglia, L. C. Skinner, A. Schmittner, Weak overturning circulation and high Southern Ocean nutrient utilization maximized glacial ocean carbon. *Earth Planet. Sci. Lett.* **496**, 47–56 (2018).
25. T. Kurahashi-Nakamura, A. Paul, M. Losch, Dynamical reconstruction of the global ocean state during the Last Glacial Maximum. *Paleoceanography* **32**, 326–350 (2017).
26. S. Gu, Z. Liu, D. W. Oppo, J. Lynch-Stieglitz, A. Jahn, J. Zhang, L. Wu, Assessing the potential capability of reconstructing glacial Atlantic water masses and AMOC using multiple proxies in CESM. *Earth Planet. Sci. Lett.* **541**, 116294 (2020).
27. J. Gottschalk, L. C. Skinner, J. Lippold, H. Vogel, N. Frank, S. L. Jaccard, C. Waelbroeck, Biological and physical controls in the Southern Ocean on past millennial-scale atmospheric CO_2 changes. *Nat. Commun.* **7**, 11539 (2016).
28. A. W. Jacobel, R. F. Anderson, S. L. Jaccard, J. F. McManus, F. J. Pavia, G. Winckler, Deep Pacific storage of respired carbon during the last ice age: Perspectives from bottom water oxygen reconstructions. *Quat. Sci. Rev.* **230**, 106065 (2020).
29. C. D. Peterson, L. E. Lisiecki, J. V. Stern, Deglacial whole-ocean $\delta^{13}C$ change estimated from 480 benthic foraminiferal records. *Paleoceanography* **29**, 549–563 (2014).
30. S. Khatiwala, A. Schmittner, J. Muglia, Air-sea disequilibrium enhances ocean carbon storage during glacial periods. *Sci. Adv.* **5**, eaaw4981 (2019).
31. H. Kobayashi, A. Abe-Ouchi, A. Oka, Role of Southern Ocean stratification in glacial atmospheric CO_2 reduction evaluated by a three-dimensional ocean general circulation model. *Paleoceanography* **30**, 1202–1216 (2015).
32. E. Galbraith, C. de Lavergne, Response of a comprehensive climate model to a broad range of external forcings: Relevance for deep ocean ventilation and the development of late Cenozoic ice ages. *Climate Dynam.* **52**, 653–679 (2019).
33. R. F. Anderson, J. P. Sachs, M. Q. Fleisher, K. A. Allen, J. Yu, A. Koutavas, S. L. Jaccard, Deep-sea oxygen depletion and ocean carbon sequestration during the last ice age. *Global Biogeochem. Cycles* **33**, 301–317 (2019).
34. M. Sarnthein, B. Schneider, P. M. Grootes, Peak glacial ^{14}C ventilation ages suggest major draw-down of carbon into the abyssal ocean. *Clim. Past* **9**, 2595–2614 (2013).
35. A. Jeltsch-Thömmes, G. Battaglia, O. Cartapanis, S. L. Jaccard, F. Joos, Low terrestrial carbon storage at the Last Glacial Maximum: Constraints from multi-proxy data. *Clim. Past* **15**, 849–879 (2019).
36. A. Marzocchi, M. F. Jansen, Global cooling linked to increased glacial carbon storage via changes in Antarctic sea ice. *Nat. Geosci.* **12**, 1001–1005 (2019).
37. K. Stein, A. Timmermann, E. Y. Kwon, T. Friedrich, Timing and magnitude of Southern Ocean sea ice/carbon cycle feedbacks. *Proc. Natl. Acad. Sci. U.S.A.* **117**, 4498–4504 (2020).
38. A. Schmittner, J. A. M. Green, S.-B. Wilmes, Glacial ocean overturning intensified by tidal mixing in a global circulation model. *Geophys. Res. Lett.* **42**, 4014–4022 (2015).
39. S.-B. Wilmes, A. Schmittner, J. A. M. Green, Glacial ice sheet extent effects on modeled tidal mixing and the global overturning circulation. *Paleoceanogr. Paleoclimatol.* **34**, 1437–1454 (2019).
40. V. Mariotti, D. Paillard, L. Bopp, D. M. Roche, N. Bouttes, A coupled model for carbon and radiocarbon evolution during the last deglaciation. *Geophys. Res. Lett.* **43**, 1306–1313 (2016).
41. L. Menviel, P. Spence, J. Yu, M. A. Chamberlain, R. J. Matear, K. J. Meissner, M. H. England, Southern Hemisphere westerlies as a driver of the early deglacial atmospheric CO_2 rise. *Nat. Commun.* **9**, 2503 (2018).
42. T. Obase, A. Abe-Ouchi, Abrupt Bølling-Allerød warming simulated under gradual forcing of the last deglaciation. *Geophys. Res. Lett.* **46**, 11397–11405 (2019).
43. H. Hasumi, "CCSR Ocean Component Model (COCO) version 4.0" (CCSR Report, Center for Climate System Research, University of Tokyo, 2006), vol. 25, 103 pp.
44. K-1 Model Developers, "K-1 coupled GCM (MIROC) description" (K-1 Technical Report, Center for Climate System Research, University of Tokyo, 2004), vol. 1.
45. A. Oka, H. Hasumi, A. Abe-Ouchi, The thermal threshold of the Atlantic meridional overturning circulation and its control by wind stress forcing during glacial climate. *Geophys. Res. Lett.* **39**, L09709 (2012).
46. M. Steele, R. Morley, W. Ermold, PHC: A global ocean hydrography with a high-quality Arctic Ocean. *J. Climate* **14**, 2079–2087 (2001).
47. P. Parekh, M. J. Follows, E. A. Boyle, Decoupling of iron and phosphate in the global ocean. *Global Biogeochem. Cycles* **19**, GB2020 (2005).
48. I. Y. Fung, S. K. Meyn, I. Tegen, S. C. Doney, J. G. John, J. K. B. Bishop, Iron supply and demand in the upper ocean. *Global Biogeochem. Cycles* **14**, 281–295 (2000).

49. M. E. Conkright, H. E. Garcia, T. D. O'Brien, R. A. Locarnini, T. P. Boyer, C. Stephens, J. I. Antonov, *World Ocean Atlas 2001, Vol. 4, Nutrients*, S. Levitus, Ed. (NOAA Atlas NESDIS, NOAA, 2002), vol. 52, 392 pp.

50. R. A. Locarnini, T. D. O'Brien, H. E. Garcia, J. I. Antonov, T. P. Boyer, M. E. Conkright, C. Stephens, *World Ocean Atlas 2001, Vol. 3, Oxygen*, S. Levitus, Ed. (NOAA Atlas NESDIS, NOAA, 2002), vol. 51, 286 pp.

51. R. M. Key, A. Kozyr, C. L. Sabine, K. Lee, R. Wanninkhof, J. L. Bullister, R. A. Feely, F. J. Millero, C. Mordy, T.-H. Peng, A global ocean carbon climatology: Results from Global Data Analysis Project (GLODAP). *Global Biogeochem. Cycles* **18**, GB4031 (2004).

52. D. Archer, Modeling the calcite lysocline. *J. Geophys. Res.* **96**, 17037–17050 (1991).

53. D. E. Archer, J. L. Morford, S. R. Emerson, A model of suboxic sedimentary diagenesis suitable for automatic tuning and gridded global domains. *Global Biogeochem. Cycles* **16**, 1017 (2002).

54. M. Chikamoto, Y. Yamanaka, Sedimentary responses to an abrupt change of biogenic silica flux by a sediment model for long timescale simulations. *J. Oceanogr.* **61**, 733–746 (2005).

55. T. Takemura, M. Egashira, K. Matsuzawa, H. Ichijo, R. O'ishi, A. Abe-Ouchi, A simulation of the global distribution and radiative forcing of soil dust aerosols at the Last Glacial Maximum. *Atmos. Chem. Phys.* **9**, 3061–3073 (2009).

56. T. L. Insua, A. J. Spivack, D. Graham, S. D'Hondt, K. Moran, Reconstruction of Pacific Ocean bottom water salinity during the Last Glacial Maximum. *Geophys. Res. Lett.* **41**, 2914–2920 (2014).

57. R. Ohgaito, A. Abe-Ouchi, R. O'ishi, T. Takemura, A. Ito, T. Hajima, S. Watanabe, M. Kawamiya, Effect of high dust amount on surface temperature during the Last Glacial Maximum: A modelling study using MIROC-ESM. *Clim. Past* **14**, 1565–1581 (2018).

58. K. E. Kohfeld, C. Le Quéré, S. P. Harrison, R. F. Anderson, Role of marine biology in glacial-interglacial CO_2 cycles. *Science* **308**, 74–78 (2005).

59. S. L. Jaccard, E. D. Galbraith, Large climate-driven changes of oceanic oxygen concentrations during the last deglaciation. *Nat. Geosci.* **5**, 151–156 (2012).

60. S. L. Jaccard, E. D. Galbraith, A. Martínez-García, R. F. Anderson, Covariation of deep Southern Ocean oxygenation and atmospheric CO_2 through the last ice age. *Nature* **530**, 207–210 (2016).

61. A. Durand, Z. Chase, T. L. Noble, H. Bostock, S. L. Jaccard, A. T. Townsend, N. L. Bindoff, H. Neil, G. Jacobsen, Reduced oxygenation at intermediate depths of the southwest Pacific during the last glacial maximum. *Earth Planet. Sci. Lett.* **491**, 48–57 (2018).

62. B. A. A. Hoogakker, H. Elderfield, G. Schmiedl, I. N. McCave, R. E. M. Rickaby, Glacial-interglacial changes in bottom water oxygen content on the Portuguese margin. *Nat. Geosci.* **8**, 40–43 (2015).

63. B. A. A. Hoogakker, Z. Lu, N. Umling, L. Jones, X. Zhou, R. E. M. Rickaby, R. Thunell, O. Cartapanis, E. Galbraith, Glacial expansion of oxygen-depleted seawater in the eastern tropical Pacific. *Nature* **562**, 410–413 (2018).

64. N. E. Umling, R. C. Thunell, Mid-depth respired carbon storage and oxygenation of the eastern equatorial Pacific over the last 25,000 years. *Quat. Sci. Rev.* **189**, 43–56 (2018).

65. Z. Lu, B. A. A. Hoogakker, C.-D. Hillenbrand, X. Zhou, E. Thomas, K. M. Gutchess, W. Lu, L. Jones, R. E. M. Rickaby, Oxygen depletion recorded in upper waters of the glacial Southern Ocean. *Nat. Commun.* **7**, 11146 (2016).

66. G. Schmiedl, A. Mackensen, Multispecies stable isotopes of benthic foraminifers reveal past changes of organic matter decomposition and deepwater oxygenation in the Arabian Sea. *Paleoceanography* **21**, PA4213 (2006).

67. D. Bunzel, G. Schmiedl, S. Lindhorst, A. Mackensen, J. Reolid, S. Romahn, C. Betzler, A multi-proxy analysis of Late Quaternary ocean and climate variability for the Maldives, Inner Sea. *Clim. Past* **13**, 1791–1813 (2017).